

# Gravity wave momentum flux in the upper mesosphere derived from OH airglow imaging measurements

Shin Suzuki<sup>1</sup>, Kazuo Shiokawa<sup>1</sup>, Yuichi Otsuka<sup>1</sup>, Tadahiko Ogawa<sup>1</sup>,  
Minoru Kubota<sup>2</sup>, Masaki Tsutsumi<sup>3</sup>, Takuji Nakamura<sup>4</sup>, and David C. Fritts<sup>5</sup>

<sup>1</sup>Solar-Terrestrial Environment Laboratory, Nagoya University, Toyokawai, Aichi 442-8507, Japan

<sup>2</sup>National Institute of Information and Communications Technology, Koganei, Tokyo 184-8795, Japan

<sup>3</sup>National Institute of Polar Research, Itabashi, Tokyo 173-8515, Japan

<sup>4</sup>Research Institute for Sustainable Humanosphere, Kyoto University, Uji, Kyoto 611-0011, Japan

<sup>5</sup>Colorado Research Associates, Division of Northwest Research Associates, Boulder, Colorado 80301, USA

(Received September 28, 2006; Revised December 28, 2006; Accepted January 24, 2007; Online published June 8, 2007)

We report procedures to identify small-scale (20–100 km) atmospheric gravity waves from OH airglow images to estimate momentum fluxes carried by the waves. We also deduce contamination of background continuum emission in OH image, by comparing a simultaneous observation of OH lines measured by the Spectral Airglow Temperature Imager (SATI). We applied the procedures to a one-night dataset obtained at Shigaraki, Japan (34.9°N, 136.1°E) on November 19, 1999. The background wind, which is essential for deriving the intrinsic parameters of gravity waves, was measured by the Middle and Upper Atmosphere (MU) radar. Contamination of background continuum emission with the OH filter was deduced to be 30%. From these procedures, we found that the gravity waves identified in the OH images were mainly propagating southward or southeastward with horizontal wavelengths of 60–90 km and apparent phase speeds of 40–80 m/s. The estimated momentum fluxes on this night was 1–15 m<sup>2</sup> s<sup>-2</sup>, with an average of 4.9 m<sup>2</sup> s<sup>-2</sup>.

**Key words:** Gravity wave, momentum flux, airglow image, mesosphere and lower thermosphere.

## 1. Introduction

Atmospheric gravity waves play important roles in both the large- and small-scale dynamics of the mesosphere and lower thermosphere (MLT) through their vertical transport of horizontal momentum (Houghton, 1978; Lindzen, 1981; Vincent, 1984; Fritts and Alexander, 2003). Wave dissipation causes turbulence and divergence of momentum flux, which leads to local heating, turbulent diffusion, and acceleration of the local mean flow. The basic mechanisms of these processes have been investigated by various remote sensing and *in situ* measurement techniques (see review by Fritts, 1984). Radars have often been used to estimate momentum fluxes (Vincent and Reid, 1983; Fritts and Vincent, 1987; Tsuda and Murayama, 1990; Nakamura *et al.*, 1993). Tsuda and Murayama (1990) studied mesospheric wind at 60–85 km from 1985 to 1988 with the Middle and Upper Atmosphere (MU) radar at Shigaraki to investigate the acceleration of mean flow by divergence of gravity wave momentum flux. They reported that the meridional momentum flux was very small throughout the year, while the zonal momentum flux was significant and showed a clear seasonal variation with a mean eastward (westward) momentum flux in summer (winter). Typical values of the zonal momentum flux were  $\sim 2$  m<sup>2</sup> s<sup>-2</sup> for wave periods from 5 min to 2 h.

For the study of gravity waves, airglow imaging is a very

useful technique. An airglow imager observes smaller scale ( $\lambda < 100$  km) gravity waves in the MLT region than those observed by radar. Owing to long-term airglow imaging, statistical analysis of small-scale gravity waves has been reported (e.g., Wu and Killeen, 1996; Taylor *et al.*, 1997; Walterscheid *et al.*, 1999; Ejiri *et al.*, 2003; Nakamura *et al.*, 2003; Suzuki *et al.*, 2004; Wrasse *et al.*, 2006). Recently, several attempts have been made to estimate momentum fluxes carried by gravity waves seen in airglow images (Swenson and Liu, 1998; Gardner *et al.*, 1999; Fritts *et al.*, 2002; Tang *et al.*, 2002, 2005a; Espy *et al.*, 2004). Fritts *et al.* (2002) analyzed a sequence of OH airglow images of breaking waves with high-intensity variance. The estimated momentum flux of their wave could be  $\sim 900$  m<sup>2</sup> s<sup>-2</sup> (maximum), which was far larger than the previous estimations based on the radar observations (largest values are typically  $\sim 30$ – $60$  m<sup>2</sup> s<sup>-2</sup>). Fritts *et al.* (2002) indicated, however, that this large value was consistent with the magnitude and timing of large-scale wind acceleration above the airglow layer.

Swenson and Liu (1998) and Swenson and Gardner (1998) derived a relation between the OH-airglow intensity variance and temperature variance to estimate the momentum flux from airglow image data. Tang *et al.* (2005a) introduced a new technique to identify high-frequency quasi-monochromatic wave components and estimated the momentum flux of the waves from all-sky OH airglow images. Their approach used two-dimensional cross periodograms of two consecutive time-differenced images to identify wave components. They estimated a one-night av-

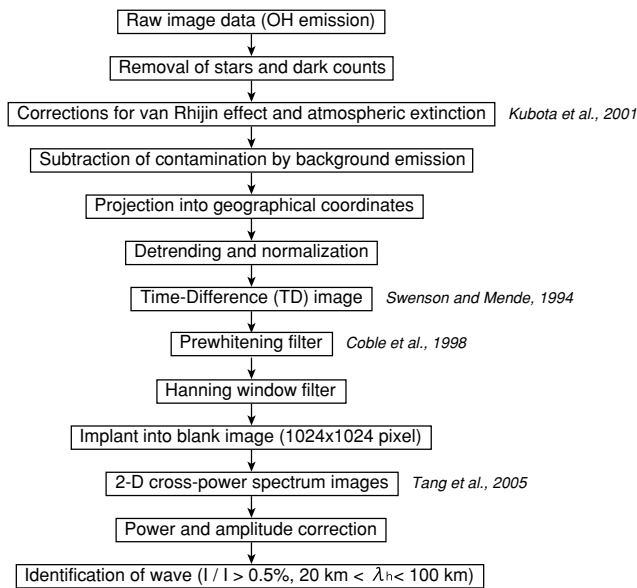


Fig. 1. Flow chart of the gravity wave extraction procedures used in the analysis.

eraged momentum flux of  $10.4 \pm 10.5 \text{ m}^2 \text{ s}^{-2}$ . Using this method with OH airglow images obtained at Maui, Hawaii ( $20.7^\circ\text{N}$ ,  $156.3^\circ\text{W}$ ), Tang *et al.* (2005b) showed seasonal variation of momentum flux, which is predominantly southwestward in winter and northeastward in summer.

In this paper, we present a technique to identify small-scale (20–100 km) gravity waves and to estimate gravity wave momentum fluxes, using one-night OH airglow images obtained at the Shigaraki MU observatory ( $34.9^\circ\text{N}$ ,  $136.1^\circ\text{E}$ ). Our method is similar to the approach of gravity wave detection presented by Tang *et al.* (2005a). We add a procedure to attenuate larger-scale ( $> 100 \text{ km}$ ) structures in the images by subtraction of a median image. Background contaminations in the OH image are deduced using the OH line spectra obtained by the Spectral Airglow Temperature Imager (SATI). The background wind data are obtained by the MU radar in meteor mode observations.

## 2. Instrumentation

The all-sky imager at Shigaraki, Japan ( $34.9^\circ\text{N}$ ,  $136.1^\circ\text{E}$ ) is part of the Optical Mesosphere Thermosphere Imagers (OMTIs) (Shiokawa *et al.*, 1999, 2000). The imager has multiple interference filters on a wheel, a fish-eye lens with a field of view of  $180^\circ$ , and a cooled-CCD camera with  $512 \times 512$  pixels. The integration time and time resolution of the OH image are 15 s and 2.5 min, respectively.

## 3. Image Processing

In this section, we describe the wave extraction processes from OH airglow images according to the flow chart shown in Fig. 1.

### 3.1 Image corrections

An airglow image contains information on various atmospheric effects, including small-scale gravity waves that we seek to study and influences of other large-scale waves as well as various image contaminations. Figure 2(a) shows an example of all-sky OH image. To extract small-scale

(20–100 km) gravity waves from the image, we needed to make several corrections to the image.

First, bright stars were attenuated from images by using a median filter, which is a common approach (Garcia *et al.*, 1997; Coble *et al.*, 1998). When the count difference between the raw pixel count and the median of the  $20 \times 20$  surrounding pixels was larger than the mean raw count of the full image, the raw count was replaced by the median count. This method offered attenuations for spike-like structures, such as stars, in the image. We also removed dark counts of the CCD. The dark counts can be estimated from the four corners of the original images, where the sky image is not projected (see Fig. 2(a)). We took the counts averaged over the four corners of the images as dark counts.

Second, we corrected for the van Rhijin effect and atmospheric extinction in the images. Airglow intensity observed by a ground-based imager is not uniform for different zenith angles, even if the airglow emission is spatially uniform. The observed intensity is proportional to the length of the line of sight (LOS) in the airglow emission layer. This is called the van Rhijin effect. On the other hand, the observed intensity is weakened by the atmospheric absorption. The amount of absorption is proportional to the length of the LOS from the emission layer to the observation point. We corrected these effects by fitting a correction factor modeled by Kubota *et al.* (2001).

We then subtracted background contamination counts for the images. The background counts are caused by emissions from the sky, including light scattered by dust, from urban areas, and from the atmospheric continuum emission, because our imager uses a filter with a broad-pass band of 720–910 nm for the measurement of the OH airglow. To obtain the actual counts from OH airglow emission, these offset counts should be removed. Swenson and Mende (1994) deduced that the background contributed to  $\sim 30\%$  of the total OH image signal, by comparing a simultaneous measurement of individual OH lines in the (8-3) band using a Fabry Perot interferometer for several nights at Bear Lake, Utah. In this paper, we deduced the background counts by using the OH airglow intensity measured simultaneously by the SATI, which was collocated with the airglow imager at Shigaraki. The SATI measures the OH airglow intensity of each OH(6-2) Q-branch emission line using a narrow-band filter (Wiens *et al.*, 1997; Shiokawa *et al.*, 2004). The SATI measures three wavelengths of  $Q_1(1)$ : 834.5 nm,  $Q_1(2)$ : 835.3 nm, and  $Q_1(3)$ : 836.5 nm, with field of view of  $30^\circ$ . We assumed that the intensities obtained by the imager could be expressed as

$$I_{\text{imager}} = A \cdot I_{\text{SATI}} + B_G, \quad (1)$$

where  $I_{\text{imager}}$ ,  $I_{\text{SATI}}$ ,  $A$ , and  $B_G$  are OH intensities measured by the airglow imager and the SATI, a proportionality constant, and the background count, respectively. We assumed that the background count was constant spatially and temporally throughout the observation period, since the observation was made during the period when the moon was not in the sky. By considering that  $I_{\text{SATI}}$  is the average intensity over the SATI field of view ( $30^\circ$ ), the value of  $I_{\text{imager}}$  was calculated by averaging the imager counts over  $256 \times 256$  pixels around the image center, after the correc-

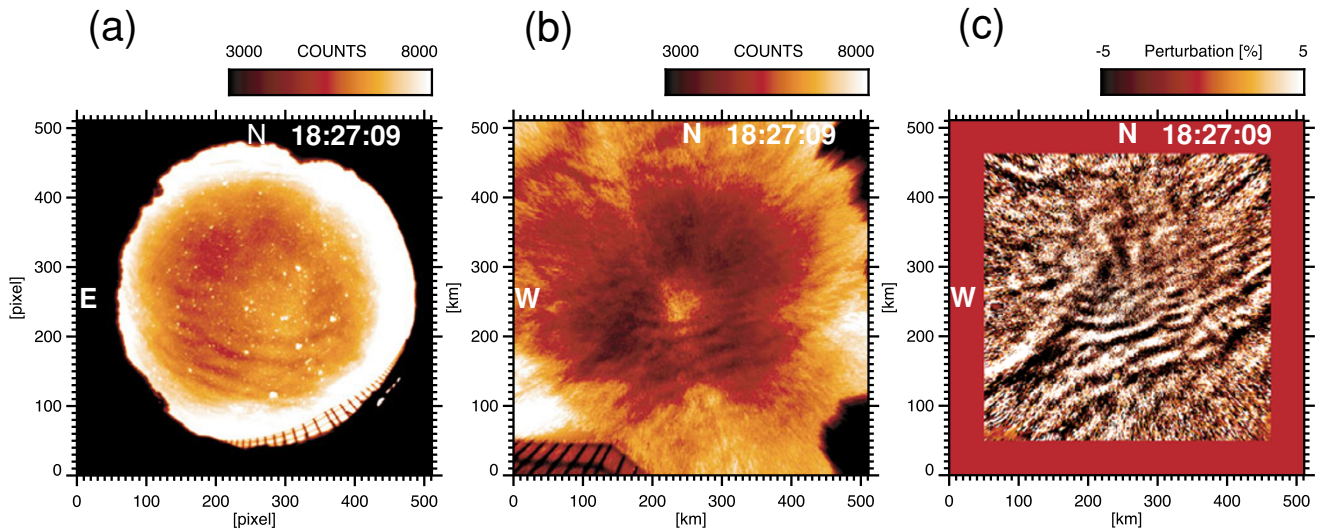


Fig. 2. (a) Example of raw all-sky OH airglow images at 1827 UT (0327 LT) obtained at Shigaraki on November 19, 1999. (b) Same as (a), except that it was a corrected intensity count projected onto the geographical grid with a size of  $512 \times 512 \text{ km}^2$ . The NNW-SSE structure in the center of the images is the Milky Way. (c) Same as (b), except that the Milky Way was removed.

tions of van Rhijn and atmospheric extinction effects.

$I_{\text{SATI}}$  and  $I_{\text{imager}}$  obtained on this night are plotted in Fig. 3(a). By a least-squares fitting of Eq. (1) to this data set, we obtained a background count of  $1558 \pm 157$  counts/pixel, in which the error was estimated from the count statistics of the images. Note that nearly 30% of the raw counts in each pixel of the images were due to the background emission and that this amount is comparable to the result deduced by Swenson and Mende (1994). Figure 3(b) shows the time evolutions in the counts obtained by the imager (solid curve with triangles) and the counts calculated from the SATI measurement using Eq. (1) with the fitted values of  $A$  and  $B_G$  (dashed curve with squares). The temporal variations of the two intensities show fairly good correspondence. We subtracted the background count  $B_G$  from each pixel count.

Finally, we projected the count-corrected airglow images into the geographical coordinates with a size of  $512 \times 512 \text{ km}^2$  by assuming the OH-layer altitude to be 86 km. The attitude of the imager was determined from the position of stars in the original image. The projected image is shown in Fig. 2(b). One pixel in this image corresponds to 1 km in the geographical coordinate system.

The Milky Way in airglow images often disturbs the spectra of the gravity wave obtained from the images. We removed the Milky Way using the following steps. First, we calculated median images with  $100 \times 100$  pixels ( $100 \times 100 \text{ km}^2$ ) in the  $512 \times 512$ -pixel geographically mapped image and subtracted the median image from the  $512 \times 512$  images. This process attenuates large-scale intensity perturbations, such as those by tides and the Milky Way. Then, the subtracted image counts  $I_s$  were normalized by the average of the whole median image counts  $I_m$ , that is,  $I_s/I_m$ . Finally, we created a time-difference (TD) image by taking the differences between two sequential images (Swenson and Mende, 1994; Haque and Swenson, 1999). The Milky Way structures move more slowly than the small-scale gravity wave in the sequential images. Thus, only the Milky Way structure was removed almost completely

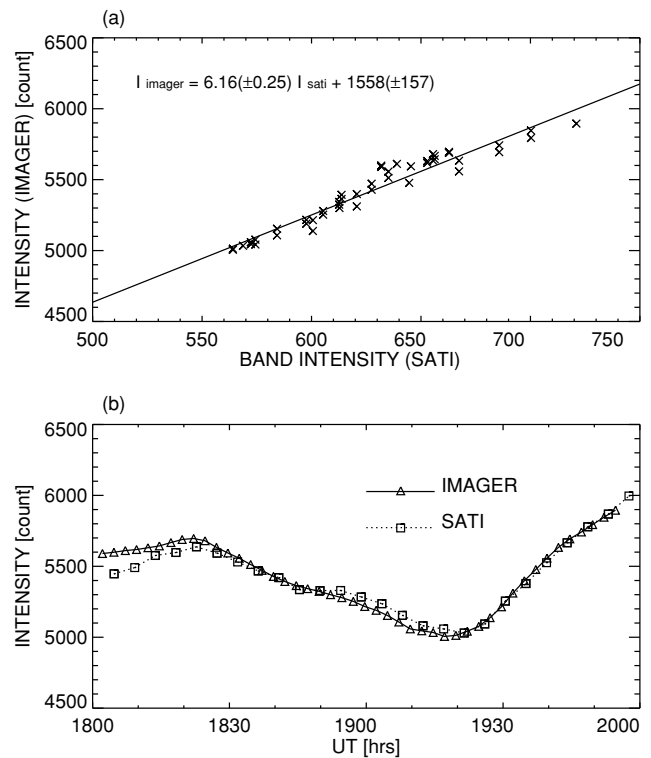


Fig. 3. (a) Relationship between the OH intensities obtained by the all-sky imager and the SATI on November 19, 1999, at Shigaraki. The solid line indicates the result of the linear least-squares fitting. The imager counts are averages of  $256 \times 256$  pixels around the zenith. (b) Temporal variations in OH intensities at 1800–2000 UT (0300–0500 LT) on November 19, 1999, at Shigaraki. Solid curve with triangles and dashed curve with squares indicate the intensities obtained by the airglow imager and the SATI, respectively. The SATI data were fitted to the imager data using the linear relation shown in (a).

by these procedures. We then made a second detrending, which is fitting a plane to the TD images and subtracting the fitted plane from the TD images, as done by Tang *et al.* (2005a). We note that while most of the Milky Way

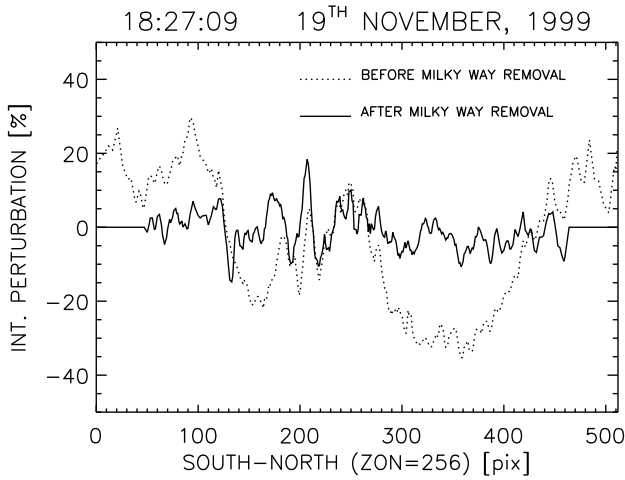


Fig. 4. Meridional cross sections along the baseline including the image center for the normalized airglow images at 1827 UT in Figs. 2(b) and (c). Dashed and solid curves are for the image before (Fig. 2(b)) and after (Fig. 2(c)) Milky Way removal.

structures are removed by the TD method, the subtraction median image we introduced above would be useful for removal of the Milky Way with significant intensity enhancement in airglow images.

Tang *et al.* (2005a) also adopted a Doppler-shifting process, for which the images before taking TD are shifted by the distance obtained by the multiplying the wind velocity and the time interval between the two images. This process can enhance the Milky Way structure in the TD image when the structure in the original image is very significant. Thus, we did not adopt the Doppler-shifting process in the present analysis.

Figure 2(c) shows the image after the Milky Way removal from Fig. 2(b). The Milky Way structure in the NNW-SSE direction was clearly removed. The edge of the image over 50 pixels cannot be processed, so the counts were set to zero. Figure 4 shows the meridional cross sections at the center of the image of Figs. 2(b) (dashed curve) and 2(c) (solid curve). The intensity enhancement caused by the Milky Way at 150–300 pixels was removed, and the image became flatter.

Note that the subtraction of the median image with  $100 \times 100 \text{ km}^2$  (smoothing) causes a wave amplitude modulation. The amount of amplitude modulation varies depending on the horizontal wavelength of the wave structure. The maximum modulation is  $\sim 50\%$  at  $\lambda_h \sim 70 \text{ km}$ . We corrected this amplitude modulation after identifying the waves, as shown in the next section.

### 3.2 Wave identification

Using spectrum analysis techniques, we identified gravity waves from the TD images and determined their zonal and meridional wavenumbers ( $k$ ,  $l$ ), horizontal wavelengths  $\lambda_h$ , apparent phase speeds  $c$ , and intensity perturbations  $I'/I$ . In the analysis, we grouped three sequential images, with each group containing two TD images. Thus, the gravity wave parameters are determined every 7.5 min.

A two-dimensional prewhitening filter, introduced by Coble *et al.* (1998), was applied to each image. We then applied a two-dimensional Hanning window to each TD im-

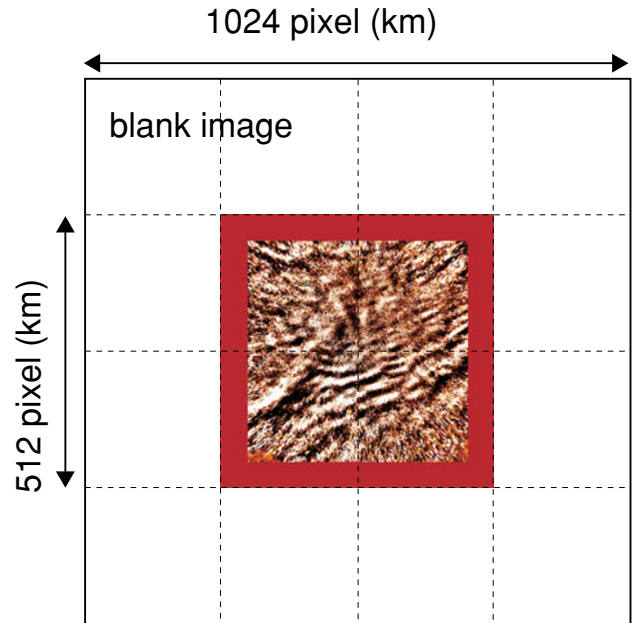


Fig. 5. Schematic picture of the TD image embedded in the double-sized blank image. The TD image is at 1824–1827 UT on November 19, 1999, at Shigaraki.

age to remove edge effects. In order to obtain gravity wave spectra with high-wavenumber resolution, each TD image was implanted at the center of a blank image with twice the size ( $1024 \times 1024$  pixels), as shown in Fig. 5. Finally, we created two two-dimensional power spectrum images and one two-dimensional cross-power spectrum image from one group, which is the same procedure adopted by Tang *et al.* (2005a).

Figure 6 shows the squared magnitude of the two-dimensional cross-power spectrum image obtained from the image in Fig. 5. Propagation direction and zonal and meridional wavenumbers are determined from the peak position of the spectra. Due to the  $180^\circ$  ambiguity for the FFT analysis, the two-dimensional spectra are revealed in both the first (second) and third (fourth) quadrants symmetrically. The  $180^\circ$  ambiguity of wave propagation is solved by calculating phase  $\theta$  of the cross-power spectrum. The apparent speeds  $c$  are calculated from the phase at the peak as:

$$c = \frac{\theta}{\Delta t} \frac{\lambda_h}{2\pi}, \quad (2)$$

where  $\Delta t$  is the time step (2.5 min in this paper) between the two TD images.

The amplitudes of intensity perturbations were computed by integrating the power over the central peaks of the power spectrum. However, corrections are required for the estimation of the amplitude, because the magnitude of the power is modified by the above image processing: i.e., detrending, TD method, prewhitening, Hanning window, and image implanting. We corrected the power using correction factors, which are obtained by numerical calculations using ideal two-dimensional sinusoidal waves.

To distinguish the peaks caused by gravity waves from noise, we adopted the criteria that individual gravity waves should have a power greater than 10% of the total spectrum

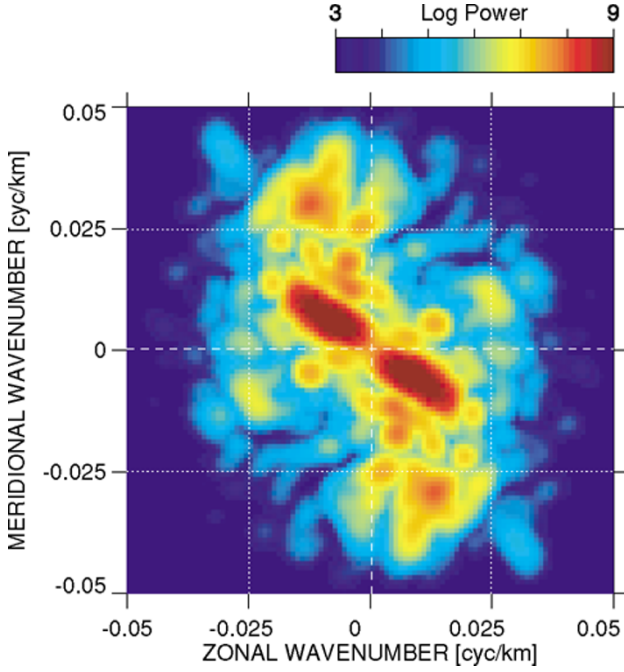


Fig. 6. Squared magnitude of the cross-power spectrum (in log scale) for the OH image at 1824–1829 UT on November 19, 1999, at Shigaraki. The positive wavenumbers in zonal and meridional directions correspond to the east and north directions, respectively.

and intensity amplitudes greater than 0.5%. It is noteworthy that multiple waves can be extracted from one group of images in our analysis as long as each wave satisfies the above criteria.

The vertical wavenumber  $m = 2\pi/\lambda_z$  was calculated from the linear dispersion relation for gravity waves,

$$m^2 = \frac{(k^2 + l^2)(N^2 - \hat{\omega}^2)}{\hat{\omega}^2 - f^2} - \frac{1}{4H^2}, \quad (3)$$

where  $N$  is the buoyancy (Brunt-Väisälä) frequency,  $\hat{\omega} = 2\pi c_i/\lambda_h$  is the intrinsic frequency (where  $c_i$  is the intrinsic phase speed),  $f = 2\Omega \sin \phi$  is the Coriolis parameter (where  $\Omega$  is the rotation rate of the earth and  $\phi$  is latitude),  $H$  is the scale height, and  $\lambda_z$  is the vertical wavelength of the gravity wave. For gravity waves having small horizontal scales and significant airglow intensity amplitudes, the intrinsic frequency is much larger than  $f$ , and the latter can safely be neglected in Eq. (3). Gravity waves having  $m^2 < 0$  do not propagate vertically, account for little or no momentum flux, and are excluded from our analysis.

In addition to the above procedures, we also set criteria on the scale of waves before the momentum flux calculation. We excluded waves with horizontal wavelengths of less than 20 km, which cannot be distinguished from structures caused by local instability, such as ripples, and those with horizontal wavelengths of more than 100 km, which cannot be quantified fully due to our procedures for removing image contamination by the Milky Way. We also excluded waves with vertical wavelengths of less than 12 km, which essentially are too small to be observed by the airglow imaging considering the thickness of the emission layer (Swenson *et al.*, 2000), and more than 60 km, which also might be ducted waves.

### 3.3 Momentum flux

The momentum flux per unit mass of gravity wave is defined as the covariance of horizontal and vertical wind perturbations. To estimate the zonal and meridional momentum flux of internal ( $m^2 > 0$ ) gravity waves, we adopted the following expressions, which were derived from the polarization relations for gravity waves having intermediate or high intrinsic frequencies (Fritts and Alexander, 2003) with cancellation factor  $C_F$  (Swenson and Gardner, 1998; Swenson and Liu, 1998; Liu and Swenson, 2003).

$$\langle u'w' \rangle = \frac{1}{2} \frac{km\hat{\omega}^2}{k^2 + l^2} \frac{g^2}{N^4 C_F^2} \left( \frac{I'}{I} \right)^2, \quad (4)$$

$$\langle v'w' \rangle = \frac{1}{2} \frac{lm\hat{\omega}^2}{k^2 + l^2} \frac{g^2}{N^4 C_F^2} \left( \frac{I'}{I} \right)^2, \quad (5)$$

where the brackets  $\langle \rangle$  indicate the average of the one wave cycle and  $g$  is the gravitational acceleration. The cancellation factor  $C_F$  connects the perturbations of temperature and OH airglow intensity as  $T'/T = (I'/I)/C_F$ , where  $T$  is undisturbed temperature,  $I$  is undisturbed volume integrated intensity, and primes denote perturbations from these means.  $C_F$  indicates that the wave perturbations in airglow intensity are reduced for small vertical wavelength due to vertical cancellation through the OH emission layer.  $C_F$  is represented as an exponential function,  $C_F = 3.5 - (3.5 - 0.01) \exp[-0.0055(\lambda_z - 6)^2]$ , where the vertical wavelength  $\lambda_z$  is in kilometers (Swenson and Liu, 1998).  $C_F$  increases monotonically with increasing  $\lambda_z$ . For small  $\lambda_z$ ,  $C_F$  decreases sharply as the cancellation effect becomes strong (Liu and Swenson, 2003). Uncertainties in  $C_F$  due to departures of the observed airglow layer from the model employed for its calculation likely represent the largest uncertainty in our computation of momentum fluxes. We note that the new  $C_F$  model has been presented by Liu and Swenson (2003), and the analytical fit for this is being implemented. The difference between the cancellation factors would result in the  $\sim 10\%$  of difference of momentum fluxes (Tang *et al.*, 2005b).

## 4. Experimental Results

We applied the procedures described above to estimate gravity wave momentum fluxes for the one-night dataset obtained at Shigaraki, Japan, on November 19, 1999 (1732–2029 UT). The background wind was measured by the meteor-mode observation of the MU radar with a time resolution of 30 min (Nakamura *et al.*, 1991).

Figure 7 shows the distributions of all gravity wave parameters inferred during this night. Typical waves had horizontal wavelengths of  $\sim 70$  km, wave periods of  $\sim 15$  min, and intensity amplitudes of  $\sim 2\%$ , and propagated largely southward or southeastward. These distributions had obvious peaks and were consistent with the behavior inferred from visual inspection, confirming the validity of our analysis procedures.

Figure 8 shows the scatter plot of momentum fluxes calculated for the night. Each point represents the total momentum flux of all wave components within each 7.5-min interval. The average zonal and meridional momentum

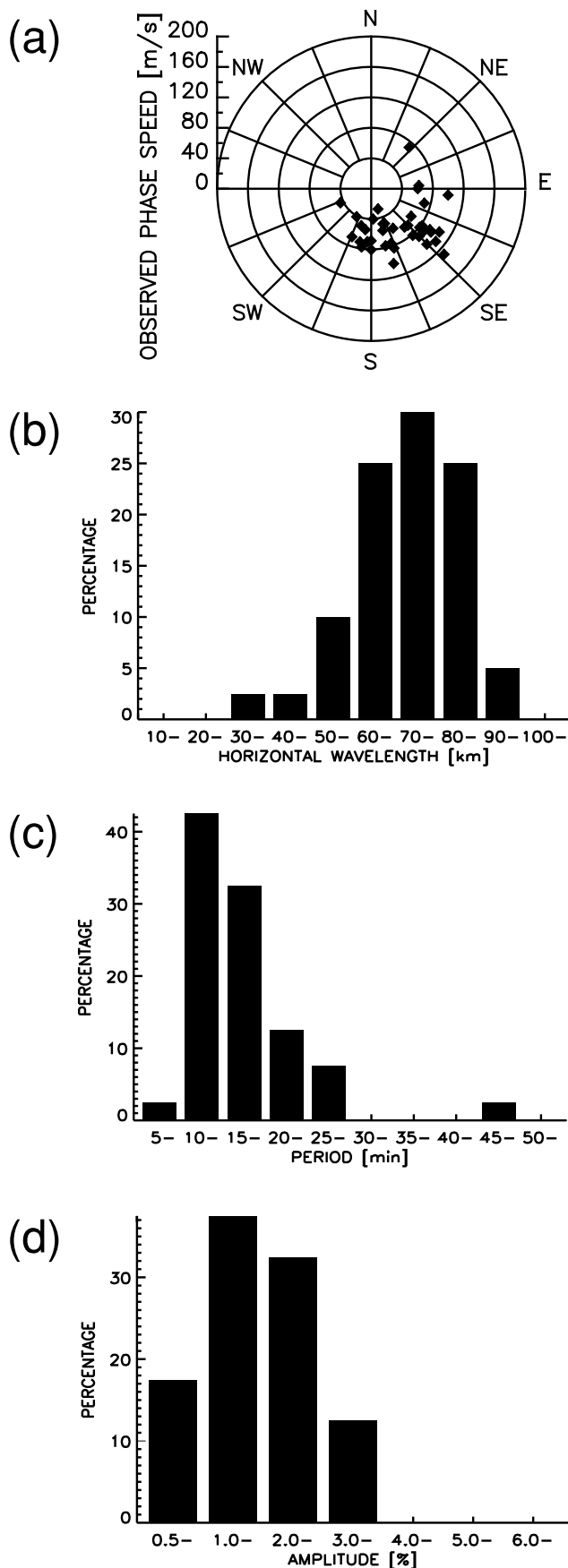


Fig. 7. Distributions of extracted gravity wave parameters on November 19, 1999, at Shigaraki. (a) Observed phase speed, (b) horizontal wavelength, (c) wave period, and (d) amplitude of intensity perturbation.

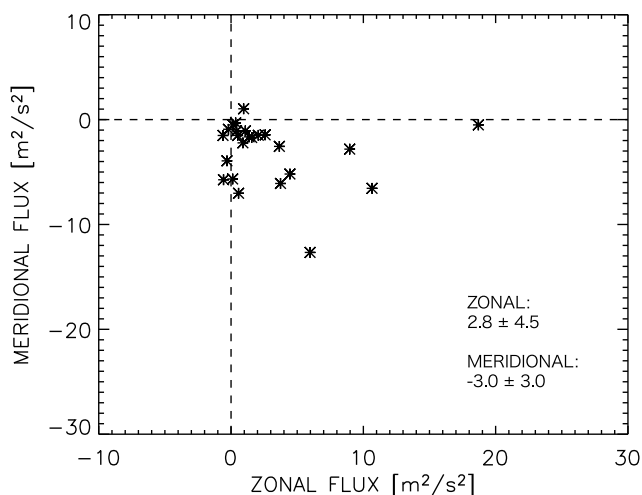


Fig. 8. Scatter plots of momentum flux on November 19, 1999, at Shigaraki. The positive momentum fluxes in zonal and meridional directions correspond to east and north directions, respectively. The average and standard deviations of the momentum flux for each direction are shown at bottom right.

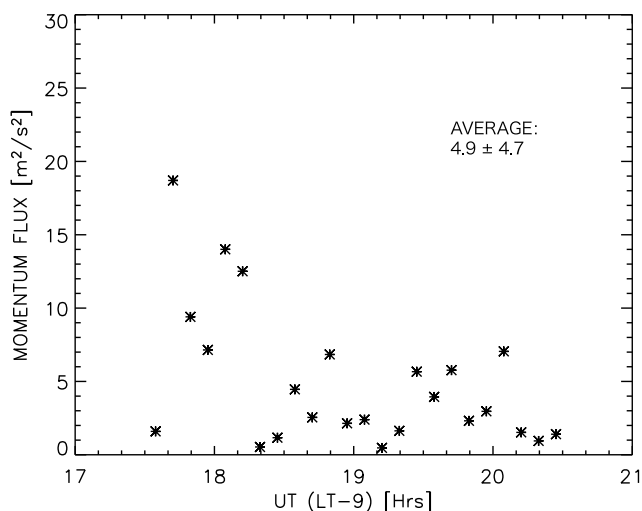


Fig. 9. Temporal variation of the estimated momentum flux.

fluxes were  $2.8 \pm 4.5 \text{ m}^2 \text{ s}^{-2}$  and  $-3.0 \pm 3.0 \text{ m}^2 \text{ s}^{-2}$ , respectively. Figure 9 shows the temporal variation of the momentum fluxes, which tend to decrease toward morning. Magnitudes varied from 1–15  $\text{m}^2 \text{ s}^{-2}$ , with average and standard deviations of  $4.9 \pm 4.7 \text{ m}^2 \text{ s}^{-2}$ .

## 5. Discussion

The magnitudes of gravity wave momentum fluxes of 1–15  $\text{m}^2 \text{ s}^{-2}$  estimated above were comparable to the results of past studies using airglow imaging. Espy *et al.* (2004) investigated gravity wave momentum flux from long-term airglow imaging observations for 2 years in Antarctica. The averages of their estimations were  $-4.4 \pm 0.6 \text{ m}^2 \text{ s}^{-2}$  (zonal) and  $0.5 \pm 0.2 \text{ m}^2 \text{ s}^{-2}$  (meridional). Fritts and Alexander (2003) noted that the mean value of gravity wave momentum flux measured by atmospheric radars was  $\sim 1\text{--}10 \text{ m}^2 \text{ s}^{-2}$ . This value is again comparable to the present result, although the airglow imager measures shorter-period and smaller-scale waves.

It is well known that the wind system in the MLT region is accelerated by gravity waves where wave dissipation and momentum flux divergence occur. Here we estimate the induced acceleration, which is expressed as

$$\frac{\partial \mathbf{u}}{\partial t} = -\frac{1}{\rho} \frac{\partial}{\partial z} \rho \mathbf{F}_M \approx \mathbf{F}_M \left( \frac{1}{H} - \frac{1}{H_E} \right), \quad (6)$$

where  $\mathbf{u}$  and  $\mathbf{F}_M$  are the mean wind and gravity wave momentum flux, respectively along the gravity wave propagation direction,  $\rho$  is the atmospheric density, and  $H_E$  is the scale height of growth of gravity wave variance (Fritts and Vincent, 1987; Fritts and VanZandt, 1993). To estimate the accelerations accompanying these gravity waves, we assume that the wave variances grow with altitude by  $\sim 2.3H$  (Fritts and VanZandt, 1993). With  $H \sim 6$  km, this yields an estimate of  $\sim 1.7 \text{ m s}^{-1} \text{ h}^{-1}$  in a southeast direction.

Nakamura *et al.* (1993) estimated that zonal and meridional drag of mean winds induced by gravity wave with periods from 5 min to 8–10 hours by the MU radar were  $51 \text{ m s}^{-1} \text{ day}^{-1}$  and  $4 \text{ m s}^{-1} \text{ day}^{-1}$  ( $4 \text{ m s}^{-1} \text{ day}^{-1}$  and  $7 \text{ m s}^{-1} \text{ day}^{-1}$ ) in June at altitude of 75 km (October at 70 km). They also suggested effects of the gravity wave on mean wind from a good correlation of the day-to-day variation in zonal momentum flux with vertical shear of the zonal mean wind. In the present analysis, the inferred acceleration by the observed wave component would amount to  $\sim 41 \text{ m s}^{-1} \text{ day}^{-1}$ , if the forcing persisted for 24 h. While such situation is unlikely to occur, airglow imager data indicate a high occurrence of small-scale gravity waves (typically more than 50%) suggesting that the small-scale gravity waves can make a significant impact on the mean wind circulation.

## 6. Summary

We have reported procedures to extract small-scale (20–100 km) gravity waves from OH airglow images using spectrum analysis techniques. This method includes procedures to remove background effects and the contamination of images by the Milky Way. We applied these methods to a one-night observation at Shigaraki, Japan, on November 19, 1999. Contamination of the airglow images by background continuum emissions was deduced to be  $\sim 30\%$ . Gravity waves observed on that night had horizontal wavelengths of 60–90 km, apparent phase speeds of 40–80 m/s, wave periods of 10–20 min, and intensity perturbations of 1–3%. Almost all waves propagated southward or southeastward. The magnitude of momentum fluxes was estimated to be  $1\text{--}15 \text{ m}^2 \text{ s}^{-2}$ . The inferred acceleration by the observed small-scale gravity wave component was  $\sim 1.7 \text{ m s}^{-1} \text{ h}^{-1}$ , and would have a potential to control the wind in the mesopause region, where waves might be dissipated. By using the procedures presented here, we can investigate day-to-day and seasonal variations of small-scale gravity waves using our long-term observations. The procedures also offer the investigation of the correspondence between wind variations and momentum flux.

**Acknowledgments.** Y. Katoh and M. Satoh are gratefully acknowledged for their skillful support in the airglow measurements. S. Suzuki is grateful to A. Z. Liu for his helpful comments and

suggestions. Support for D. Fritts was provided under NASA contract NAS5-02036. The MU radar belongs to and is operated by the Research Institute for Sustainable Humanosphere, Kyoto University. This work was supported by a Grant-in-Aid for Scientific Research of the Ministry of Education, Culture, Sports, Science and Technology of Japan (11440145, 13573006, and Priority Area 764) and Dynamics of the Sun-Earth-Life Interactive System (No. G-4, the 21st Century COE Program). S. Suzuki is supported by a Grant-in-Aid for JSPS Fellows (17-7673) of the Ministry of Education, Culture, Sports, Science and Technology of Japan.

## References

- Coble, M. R., G. C. Papen, and C. S. Gardner, Computing two-dimensional unambiguous horizontal wavenumber spectra from OH airglow images, *IEEE Trans. Geosci. Remote Sens.*, **36**, 368–382, 1998.
- Ejiri, M. K., K. Shiokawa, T. Ogawa, K. Igarashi, T. Nakamura, and T. Tsuda, Statistical study of short-period gravity waves in OH and OI nightglow images at two separated sites, *J. Geophys. Res.*, **108**(D21), 4679, doi:10.1029/2002JD002795, 2003.
- Espy, P. J., G. O. L. Jones, G. R. Swenson, J. Tang, and M. J. Taylor, Seasonal variations of the gravity wave momentum flux in the Antarctic mesosphere and lower thermosphere, *J. Geophys. Res.*, **109**, D23109, doi:10.1029/2003JD004446, 2004.
- Fritts, D. C., Gravity wave saturation in the middle atmosphere: A review of theory and observations, *Rev. Geophys. Space Sci.*, **22**, 275–308, 1984.
- Fritts, D. C. and T. E. VanZandt, Spectral estimates of gravity wave energy and momentum fluxes. Part I: Energy dissipation, acceleration, and constraints, *J. Atmos. Sci.*, **50**, 3685–3694, 1993.
- Fritts, D. C. and R. A. Vincent, Mesospheric momentum flux studies at Adelaide, Australia: Observations and a gravity wave-tidal interaction model, *J. Atmos. Sci.*, **44**, 605–619, 1987.
- Fritts, D. C., S. L. Vadas, and Y. Yamada, An estimate of strong local body forcing and gravity wave radiation based on OH airglow and meteor radar observations, *Geophys. Res. Lett.*, **29**, doi:10.1029/2001GL013753, 2002.
- Fritts, D. C. and M. J. Alexander, Gravity wave dynamics and effects in the middle atmosphere, *Rev. Geophys.*, **41**(1), 1003, doi:10.1029/2001RG000106, 2003.
- Garcia, F. J., M. J. Taylor, and M. C. Kelley, Two-dimensional spectral analysis of mesospheric airglow image data, *Appl. Opt.*, **36**, 7374–7385, 1997.
- Gardner, C. S., K. Gulati, Y. Zhao, and G. R. Swenson, Measuring gravity wave momentum fluxes with airglow images, *J. Geophys. Res.*, **104**, 11,903–11,915, 1999.
- Haque, R. and G. R. Swenson, Extraction of motion parameters of gravity-wave structures from all-sky OH image sequences, *Appl. Opt.*, **38**, 4433–4442, 1999.
- Houghton, J. T., The stratosphere and mesosphere, *Quart. J. R. Met. Soc.*, **104**, 1–29, 1978.
- Kubota, M., H. Fukunishi, and S. Okano, Characteristics of medium- and large-scale TIDs over Japan derived from OI 630-nm nightglow observation, *Earth Planets Space*, **53**, 741–751, 2001.
- Lindzen, R. S., Turbulence and stress owing to gravity wave and tidal breakdown, *J. Geophys. Res.*, **86**, 9707–9714, 1981.
- Liu, A. Z. and G. R. Swenson, A modeling study of O<sub>2</sub> and OH airglow perturbations induced by atmospheric gravity waves, *J. Geophys. Res.*, **108**(D4), 4151, doi:10.1029/2002JD002474, 2003.
- Nakamura, T., T. Tsuda, T. Tsutsumi, K. Kita, T. Uehara, S. Kato, and S. Fukao, Meteor wind observations with the MU radar, *Radio Sci.*, **26**, 857–869, 1991.
- Nakamura, T., T. Tsuda, M. Yamamoto, S. Fukao, and S. Kato, Characteristics of gravity waves in the mesosphere observed with the middle and upper atmosphere radar 1. Momentum flux, *J. Geophys. Res.*, **98**, 8899–8910, 1993.
- Nakamura, T., T. Aono, T. Tsuda, A. G. Admiranto, E. Achmad, and Suratno, Mesospheric gravity waves over a tropical convective region observed by OH airglow imaging in Indonesia, *Geophys. Res. Lett.*, **30**, 1882, doi:10.1029/2003GL017619, 2003.
- Shiokawa, K., Y. Katoh, M. Satoh, M. K. Ejiri, and T. Ogawa, Development of optical mesosphere thermosphere imagers, *Earth Planets Space*, **51**, 887–896, 1999.
- Shiokawa, K., Y. Katoh, M. Satoh, M. K. Ejiri, and T. Ogawa, Integrating-sphere calibration of all-sky cameras for nightglow measurements,

- Adv. Space Res.*, **26**, 1025–1028, 2000.
- Shiokawa, K., Y. Otsuka, T. Ogawa, H. Takahashi, T. Nakamura, and T. Shimomai, Comparison of OH rotational temperatures measured by the spectral airglow temperature imager (SATI) and by a tilting-filter photometer, *J. Atmos. Terr. Phys.*, **66**, 891–897, 2004.
- Suzuki, S., K. Shiokawa, Y. Otsuka, T. Ogawa, and P. Wilkinson, Statistical characteristics of gravity waves observed by an all-sky imager at Darwin, Australia, *J. Geophys. Res.*, **109**(D20S07), doi:10.1029/2003JD004336, 2004.
- Swenson, G. R. and C. S. Gardner, Analytical models for the responses of the mesospheric OH\* and Na layers to atmospheric gravity waves, *Geophys. Res. Lett.*, **25**, 477–480, 1998.
- Swenson, G. R. and A. Z. Liu, A model for calculating acoustic gravity wave energy and momentum flux in the mesosphere from OH airglow, *J. Geophys. Res.*, **103**, 6271–6294, 1998.
- Swenson, G. R. and S. B. Mende, OH emission and gravity waves (including a breaking wave) in all-sky imagery from Bear Lake, UT, *Geophys. Res. Lett.*, **21**, 2239–2242.
- Swenson, G. R., M. J. Alexander, and R. Haque, Dispersion imposed limits on atmospheric gravity waves in the mesosphere: Observations from OH airglow, *Geophys. Res. Lett.*, **27**, 875–878, 2000.
- Tang, J., A. Z. Liu, and G. R. Swenson, High frequency gravity waves observed in OH airglow at Starfire Optical Range, NM: Seasonal variations in momentum flux, *Geophys. Res. Lett.*, **29**(20), 1996, doi:10.1029/2002GL015794, 2002.
- Tang, J., F. Kamalabadi, S. J. Franke, A. Z. Liu, and G. R. Swenson, Estimation of gravity wave momentum flux with spectroscopic imaging, *IEEE Trans. Geosci. Remote Sens.*, **43**, 103–109, 2005a.
- Tang, J., G. R. Swenson, A. Z. Liu, and F. Kamalabadi, Observational investigations of gravity wave momentum flux with spectroscopic imaging, *J. Geophys. Res.*, **110**, D09S09, doi:10.1029/2004JD004778, 2005b.
- Taylor, M. J., W. R. Pendleton Jr., S. Clark, H. Takahashi, D. Gobbi, and R. A. Goldberg, Image measurements of short-period gravity waves at equatorial latitudes, *J. Geophys. Res.*, **102**, 26,283–26,299, 1997.
- Tsuda T. and Y. Murayama, Seasonal variation of momentum flux in the mesosphere observed with the MU radar, *Geophys. Res. Lett.*, **17**, 725–728, 1990.
- Vincent, R. A., Gravity-wave motions in the mesosphere, *J. Atmos. Terr. Phys.*, **46**, 119–128, 1984.
- Vincent, R. A. and I. M. Reid, HF doppler measurements of mesospheric gravity wave momentum fluxes, *J. Atmos. Sci.*, **40**, 1321–1333, 1983.
- Walterscheid, R. L., J. H. Hecht, R. A. Vincent, I. M. Reid, J. Woithe, and M. P. Hickey, Analysis and interpretation of airglow and radar observations of quasi-monochromatic gravity waves in the upper mesosphere and lower thermosphere over Adelaide, Australia (35°S, 138°E), *J. Atmos. Terr. Phys.*, **61**, 461–478, 1999.
- Wiens, R. H., A. Moise, S. Brown, S. Sargoytchev, R. N. Peterson, G. G. Chepherd, M. J. López-González, J. J. López-Moreno, and R. Rodrigo, SATI: A spectral airglow temperature imager, *Adv. Space Res.*, **19**, 677–680, 1997.
- Wrasse, C. M., T. Nakamura, T. Tsuda, H. Takahashi, A. F. Medeiros, M. J. Taylor, D. Gobbi, A. Salatun, Suratno, E. Achmad, and A. G. Admiranto, Reverse ray tracing of the mesospheric gravity waves observed at 23°S (Brazil) and 7°S (Indonesia) in airglow imagers, *J. Atmos. Terr. Phys.*, **68**, 163–181, 2006.
- Wu, Q. and T. L. Killeen, Seasonal dependence of mesospheric gravity waves (< 100 km) at Peach Mountain Observatory, Michigan, *Geophys. Res. Lett.*, **23**, 2211–2214, 1996.

---

S. Suzuki (e-mail: shin@stelab.nagoya-u.ac.jp), K. Shiokawa, Y. Otsuka, T. Ogawa, M. Kubota, M. Tsutsumi, T. Nakamura, and D. C. Fritts